ACS APPLIED MATERIALS & INTERFACES

Research Article

www.acsami.org

Hybrid Bulk Heterojunction Solar Cells Based on the Cooperative Interaction of Liquid Crystals within Quantum Dots and Diblock Copolymers

Yueqin Shi,[†] Fan Li,[†] Licheng Tan,[†,‡] and Yiwang Chen*[,†,‡]

[†]Institute of Polymers/Department of Chemistry and [‡]Jiangxi Provincial Key Laboratory of New Energy Chemistry, Nanchang University, 999 Xuefu Avenue, Nanchang, Jiangxi 330031, China

Supporting Information

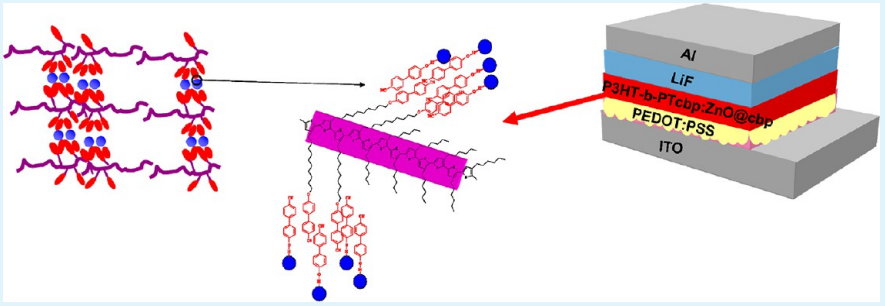

ABSTRACT: In this article, the conjugated rod−rod polythiophene diblock copolymers comprising a regioregular poly(3-hexylthiophene) (P3HT) segment and a side-chain liquid-crystalline polythiophene segment bearing cyanobiphenyl mesogenic pendants (PTcbp), polythiophene-*b*-poly{3-[10-(4′-cyanobiphenyloxy)decyl]thiophene} (P3HT-*b*-PTcbp), were rationally designed and synthesized. It was observed that the diblock copolymers could self-assemble into high crystalline and oriented nanofibrils upon 1,2-dichlorobenzene solvent vapor annealing, originating from the crystallization of two segments and the orientation of cyanobiphenyl side-chain mesogens. Hybrid bulk heterojunction (BHJ) solar cells were then fabricated using P3HT-*b*-PTcbp as electron donors and ZnO and CdS quantum dots (QDs) modified by 4′-hydroxy-[1,1′-biphenyl]-4-carbonitrile (cbp) liquid-crystalline ligands (cbp@ZnO and cbp@CdS) as electron acceptors. The interaction between the cbp ligands on the surface of ZnO and CdS QDs and cyanobiphenyl side-chain mesogens of diblock copolymers promoted the cooperative self-assembly and controllable well-dispersion of QDs in the polymer matrix and, as a consequence, yielded an intimately contacted polymer−QD nanocomposites. The power conversion efficiency (PCE) of the device based on P3HT-*b*-PTcbp/cbp@ZnO hybrids was improved by 2.6 times compared with that of P3HT/ZnO hybrids from 0.58 to 0.97. In addition, an overall PCE of a homologous device based on the P3HT-*b*-PTcbp/cbp@CdS hybrid active layer reached 2.3%. The research paved the way for the further development of high-efficiency hybrid BHJ solar cells by introducing block copolymer nanofibrils with favored crystalline domain orientations and liquid-crystalline organization properties.

KEYWORDS: *diblock copolymer, liquid crystals, quantum dots, self-assembly, hybrid solar cells*

1. INTRODUCTION

Quantum dots (QDs) are promising as electron acceptors in organic/inorganic hybrid bulk heterojunction (BHJ) solar cells for their ability to accurately tune the optical band gap simply by tuning the QD size, high electron mobility, high optical stability, strong fluorescence quantum yield, and fine physical and chemical stability.[1−5] The basic principle of organic/inorganic hybrid BHJ solar cells is exhibited as follows. Upon photon absorption, the excitons are separated at the conjugated polymer (electron donor)/QD (electron acceptor) interface into free electrons and holes, which then transport through conjugated polymer and QD phases, respectively, and finally are collected at the electrodes. The photovoltaic performance is determined by light absorption, exciton diffusion, charge dissociation at the donor/acceptor interface, and charge transfer to the respective electrode effectively. Two key challenges that limit the design of efficient hybrid BHJ solar cells are as follows: (a) charge separation at the conjugated polymer/QD interface must be fast and efficient enough to compete with decays of the excitons and (b) the interpenetrating network of QDs could be obtained to enhance charge-carrier transport and charge collection at the respective electrodes. Therefore, high electron and hole mobility, controllable nanomorphology, and a fine-structured interface are critical factors for developing efficient hybrid BHJ solar cells.

Conjugated polymers usually can provide various properties, such as well film-forming ability and solubility in different

Received: August 9, 2013
Accepted: October 21, 2013
Published: October 22, 2013

solvents, while the solubility of QDs in organic solvents is quite poor. Therefore, it is worth noting that developing routes to control the nanoscale organization of QDs in hybrid BHJ solar cells is critical to acquiring good photovoltaic performances. During the last decade, significant progress has been made in the self-assembly of QDs,[6−17] such as external field application,[18] assembly guided by DNA, and the use of liquid-crystalline ligands, surfactants, and block copolymers.[19] Among them, conjugated copolymers provide an ideal platform for driving the assembly of QDs because they can self-assemble into various fine-defined arrays of nanomorphologies through phase separation.[18−22] Meanwhile, the QDs have the tendency to grow larger easily because of the high surface energy of QDs. A proper interaction between QDs and copolymers can prevent the aggregation and oxidation of QDs, enhance the solubility of QDs, and even change the dispersion characteristics of QDs to polymer matrixes.[23] Seferos et al. found that the rod−rod conjugated diblock copolymer has the ability to co-self-assemble spherical CdSe nanocrystals by using the selenophene−thiophene diblock copolymers with various molecular weights.[19] Watkins et al. illustrated that the addition of nanoparticles, which selectively hydrogen bond with one of the block copolymer segments, could drive the nanoparticle assembly and presented a simple route to obtain ordered hybrid materials.[24,25] Xu et al. also investigated whether the block-copolymer-based supramolecules could induce nanorod assembly and showed that this approach could be used to obtain morphological control in nanorod-containing nanocomposites toward the fabrication of optical and electronic devices.[18] Additional efforts, such as Krüger et al. applying end-group functionalization of poly(3-hexylthiophene)s (P3HTs) as an efficient route to photosensitization of nanocrystalline titanium oxide (TiO_2) films for photovoltaic device applications,[26] Fréchet et al. utilizing amine-terminated P3HTs to control the morphology of a polymer−nanocrystal composite in hybrid solar cells,[27] and Kochemba et al. employing pyridine-capped P3HTs to direct the dispersion of CdSe nanocrystals,[28] were also highly relevant.

Recently, there was some research and development with regard to the control of microphase separation of block copolymers with the help of liquid-crystalline ordering.[29,30] Yu et al. pointed out that the liquid-crystalline block copolymers could supramolecularly assemble into ordered nanomorphology with high regularity by combining the liquid-crystalline elastic deformation and microphase separation of block copolymers.[31] Zhao et al. synthesized a diblock copolymer comprising a regioregular P3HT segment and a side-chain liquid-crystalline polymer segment bearing azobenzene mesogens and achieved highly oriented nanofibrils of regioregular P3HT via block copolymer self-assembly in liquid crystals.[32] Although there was considerable interest in the co-self-assembly of block copolymers with QDs for optical and electronic applications, conjugated rod−rod diblock copolymers bearing side-chain mesogens had not been applied in hybrid BHJ solar cells. On the other hand, previously it had been demonstrated that photoinduced charge transfer can occur between a conjugated polymer and zinc oxide (ZnO) QDs effectively.[33−35] ZnO has various characteristics, for instance, easy synthesis, low cost, high mobility, and tunable morphology.[33] In our research, we fabricate hybrid BHJ solar cells by using ZnO QDs modified with liquid-crystalline ligands, 4′-hydroxy-[1,1′-biphenyl]-4-carbonitrile (cbp), as electron acceptors and conjugated rod−rod diblock copolymers comprising a regioregular P3HT segment and a side-chain liquid-crystalline polythiophene segment bearing cyanobiphenyl mesogenic pendants (PTcbp), polythiophene-*b*-poly{3-[10-(4′-cyanobiphenyloxy)-decyl]thiophene} (P3HT-*b*-PTcbp), as electron donors. Because of the self-assembly and crystallinity of each conjugated segment and the interaction between the cbp ligands on the surface of ZnO QDs and cyanobiphenyl side-chain mesogens of P3HT-*b*-PTcbp, we expect to observe fine dispersion and self-assembly of ZnO QDs in a polymer matrix, an intimate contact between the conjugated polymer and QD phases, and improvement of the photovoltaic properties of the hybrid devices. The research paved the way for the further development of high-efficiency hybrid BHJ solar cells by introducing block copolymer nanofibrils with favored crystalline domain orientations and liquid-crystalline organization properties and narrow-band-gap inorganic QDs. So, we further investigate our research by applying this conjugated rod−rod diblock copolymer and another narrow-band-gap CdS QDs as the active layer to fabricate a homologous device.

2. DEVICE FABRICATION

All of the devices were fabricated with a structure of glass/ITO/PEDOT:PSS/active layer/LiF/Al. The conductive indium−tin oxide (ITO) substrates were cleaned in acetone, soapy water, deionized water, and isopropyl alcohol successively by ultrasonication. After the ITO substrate was dried and treated with UV ozone for 20 min, poly(3,4-ethylenedioxythiophene):polystyrenesulfonate (PEDOT:PSS) as the hole-transport layer was spin-coated onto the surface of ITO at a spin speed of 4000 rpm for 1 min and then thermally annealed at 140 °C for 20 min. Subsequently, the 1,2-dichlorobenzene (DCB) solution of P3HT-*b*-PTcbp (10 mg/mL) and ZnO or CdS QDs modified with cbp (1:2 weight ratio) was spin-coated onto the substrate as the active layer (∼120 nm) at a spin speed of 800 rpm for 1 min. The devices were then treated with solvent annealing in an atmosphere of DCB-saturated vapor for 10 h in a glovebox filled with nitrogen. Finally, lithium fluoride (LiF; 0.7 nm) followed by a layer of aluminum (Al; 100 nm) was deposited onto the active layer as the cathode electrode in a vacuum chamber. The current−voltage (J−V) curves of the devices were all measured under 100 mW/cm^2, AM1.5 solar irradiation in ambient air. The cell area was 4 mm^2.

3. CHARACTERIZATIONS

The NMR spectra were all recorded on a Bruker ARX 600 NMR spectrometer in a deuterated chloroform (CF) solvent, with tetramethylsilane (δ = 0) applied as the internal standard. Molecular weight distributions of P3HT-*b*-PTcbp diblock copolymers were proceed by gel permeation chromatography (from tetrahydrofuran). The IR spectra were collected using potassium bromide (KBr) substrates on a Shimadzu IRPrestige-21 Fourier transform infrared (FT-IR) spectrophotometer. UV−vis absorption spectroscopy of all samples was conducted to test the optical properties of the films and measured on a Perkin Elmer Lambda 750s spectrophotometer. Photoluminescence (PL) measurements of all samples were carried out to measure the charge transfer between conjugated copolymers and inorganic QDs on a Shimadzu RF-5301 PC spectrofluorophotometer, and the light source was a xenon lamp. The liquid-crystal characteristics of P3HT-*b*-PTcbp diblock copolymers bearing side-chain mesogens were measured through texture observations by polarizing optical microscopy (POM) with a Nikon E600POL polarizing optical microscope, which was equipped with an Instec HS 400 cooling and heating stage instrument. The crystalline properties of all samples were determined by an X-ray diffraction (XRD) study, which was carried out on a Bruker D 8 Focus X-ray

Scheme 1. Synthesis of P3HT-*b*-PTcbp Diblock Copolymers

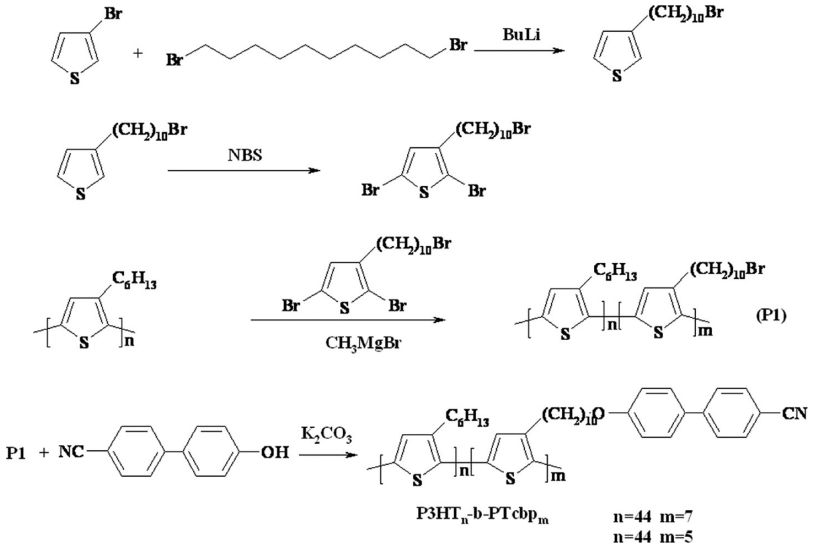

diffractometer operating at 20 mA and 30 kV with a copper target (λ = 1.54 Å) at a scan rate of 1 °C/min. The films were all spin-coated on the glass substrate. The bulk small-angle X-ray scattering (SAXS) measurements of the samples were performed to further test the crystalline morphology and recorded on a SAXSess mc^2 Anton Paar Co., Ltd., operating at 50 mA and 40 kV from Austria with no carrier. All of the samples were prepared under solvent annealing conditions by drying the polymer films in a Teflon beaker in a saturated vapor atmosphere of DCB. A Nanoscope III A (Digital Instruments) scanning probe microscope was used to investigate the surface nanomorphology of films with atomic force microscopy (AFM) images (tapping mode). Scanning electron microscopy (SEM) was applied to measure the assembly properties of the active layer and processed on a FEI, QuanTA-200F, with gold vapor deposition. Field-emission transmission electron microscopy (TEM) employed on a JEOL, JEM-2100F, was also used to observe polymers and active-layer nanostructures. The $J-V$ characteristics of the unencapsulated hybrid BHJ solar cells were measured in air using a Keithley 2400 source meter under 100 mW/cm^2 simulated AM1.5G irradiation (Abet Solar Simulator Sun2000).

4. RESULTS AND DISCUSSION

We presented the Grignard metathesis polymerization approach for synthesizing P3HT and the P3HT-*b*-poly[3-(10-bromodecyl)thiophene] (P1) diblock copolymer with different block ratios, as shown in Scheme 1. Then the precursory diblock copolymer bearing bromide end-terminated lateral chains (P1) was substituted with cbp by Williamson ether reaction to obtain polythiophene-*b*-poly{3-[10-(4′-cyanobiphenyloxy)decyl]thiophene} (P3HT-*b*-PTcbp; see the details in the Supporting Information, SI). ^{1}H and ^{13}C NMR spectra confirmed the successful synthesis of P3HT-*b*-PTcbp diblock copolymer with various block ratios, as seen in Figure 1S in the SI, which was testified by the disappearance of the peak at δ 3.71 assigned to the CH_2 protons linked to bromide. However, it should be mentioned that incomplete substitution of the bromide in the thiophene main chain would occur when the molar proportion between the poly[3-(10-bromodecyl)-thiophene] and P3HT blocks was over 7:44 in our experiments. Therefore, we only synthesized the rod−rod diblock copolymers with two different ratios, i.e., P3HT$_{44}$-*b*-PTcbp$_7$ and P3HT$_{44}$-*b*-PTcbp$_5$.

The self-assembly behavior in the rod−rod block copolymer bearing side-chain mesogens might originate from the crystallinity of rodlike segments, phase separation of a block copolymer, side-chain liquid-crystalline ordering, or the interaction between microphase separation and liquid-crystalline elastic deformation in a block copolymer.[20,21] To investigate the influence of cyanobiphenyl side-chain mesogens on the self-assembly properties of the P3HT-*b*-PTcbp, the thermal transition and mesomorphic behavior of the rod−rod diblock copolymer were studied by differential scanning calorimetry (DSC) and POM (Figure 1). From the POM images, it can be seen that the block copolymers P3HT$_{44}$-*b*-PTcbp$_7$ and P3HT$_{44}$-*b*-PTcbp$_5$ did not develop obviously characteristic optical textures, and consequently the mesophase behavior of the block copolymers containing side-chain mesogens could not clearly be identified. At the same time, DSC analysis demonstrated that the P3HT homopolymer showed only one melting transition at 213 °C, while the block copolymer P3HT-*b*-PTcbp exhibited two distinct melting temperatures (T_m), which were 225 and 240 °C for P3HT$_{44}$-*b*-PTcbp$_7$ and 215 and 240 °C for P3HT$_{44}$-*b*-PTcbp$_5$, respectively. The low T_m corresponded to the contribution of the P3HT segment and the high T_m to the PTcbp block. The results indicated that the introduction of cyanobiphenyl mesogens into diblock copolymers could result in an increase of the isotropization temperature of P3HT segments (213 °C) to 215 or 225 °C. However, the mesophase−isotropic and solid−mesophase transitions of the side-chain mesogens could not be observed in the measurements, reflecting that side-chain mesogens of the rod−rod block copolymers were too weak to induce the mesogenic behavior of the polymers. Therefore, we assumed that the self-assembly behavior of the block copolymer mainly arose from two semicrystalline chains that were linked covalently.

Figure 2 shows the normalized UV−vis spectra of P3HT, P1, P3HT$_{44}$-*b*-PTcbp$_5$, and P3HT$_{44}$-*b*-PTcbp$_7$ thin films spin-coated from CF and DCB. Compared with the pristine P3HT, the absorption peaks of P1 were red-shifted a little, while the peaks of P3HT$_{44}$-*b*-PTcbp$_5$ and P3HT$_{44}$-*b*-PTcbp$_7$ films were obviously red-shifted by a few nanometers; meanwhile, the intensity of the shoulder peak at about 610 nm was stronger and the spectra were also broader, which was

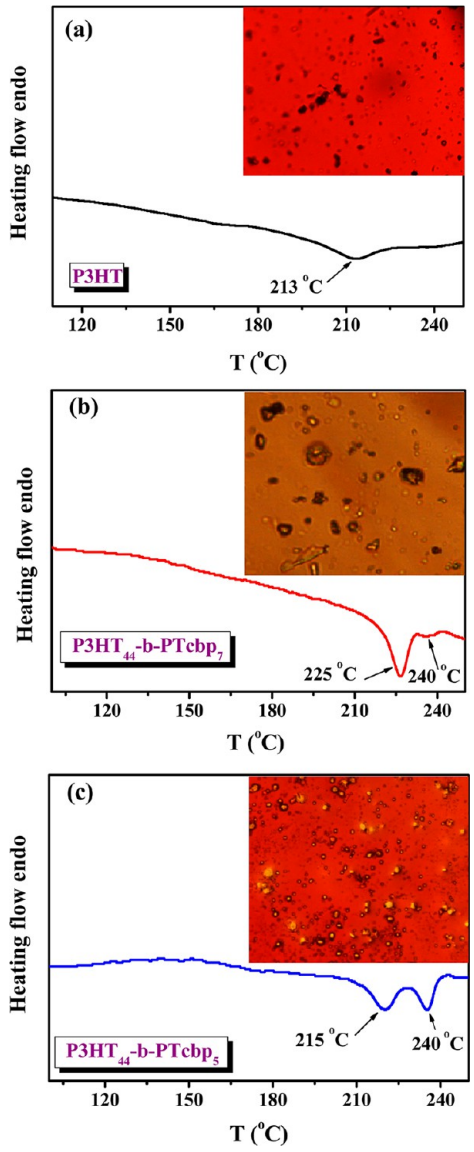

Figure 1. DSC thermograms of (a) P3HT, (b) P3HT$_{44}$-*b*-PTcbp$_7$, and (c) P3HT$_{44}$-*b*-PTcbp$_5$ recorded under nitrogen during second heating scans at a scan rate of 20 °C/min. The mesomorphic textures observed by POM at 230 °C under cooling from the melt state (cooling rate: 1 °C/min).

ascribed to the increased conjugation length, enhanced interaction of the polymer chains, and higher degree of crystallinity.[36,37] On the other hand, we also used the diblock copolymer P1 without the mesogen as a comparison, which would clearly show that it might be the synergistic effect of the orientation of cyanobiphenyl side-chain mesogens as well as the crystallizable block of the diblock copolymer driving the enhancement in the morphological and photophysical properties. In our experiment, the red shift, stronger peak intensity at 610 nm, and broader absorption of the UV−vis spectra for P3HT$_{44}$-*b*-PTcbp$_5$ and P3HT$_{44}$-*b*-PTcbp$_7$ might be attributed to the self-assembly of conjugated segments and the orientation of cyanobiphenyl side-chain mesogens in the block copolymers, which could help the block copolymers assemble into ordered nanostructures with high regularity compared with pristine P3HT. Moreover, we also observe that all films spin-casted from DCB showed larger red shifts than the films spin-casted

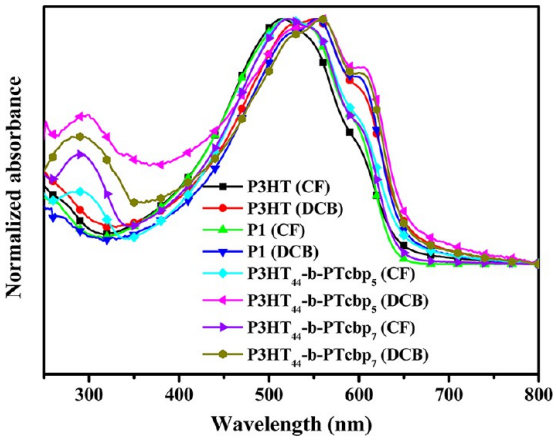

Figure 2. UV−vis spectra of pristine P3HT, P1, P3HT$_{44}$-*b*-PTcbp$_5$, and P3HT$_{44}$-*b*-PTcbp$_7$ films prepared by spin coating from CF and DCB solvents. All of the polymer concentrations were 10 mg/mL in the solutions.

from CF, suggesting that high volatile CF processing often led to the formation of random structures. On the other hand, low volatile DCB processing resulted in high crystalline structures of the block copolymers mainly because there is more time for diblock copolymer chains to rearrange during the drying process.[38,39] In addition, we could calculate the optical band gaps of 1.97, 1.85, and 2.04 eV for P3HT, P3HT$_{44}$-*b*-PTcbp$_5$, and P3HT$_{44}$-*b*-PTcbp$_7$, respectively, from the onset of polymer thin-film absorptions (Table 1).

It was well established that the nanoscale structures of conjugated copolymer films were crucial in determining the ultimate device application.[40,41] Tapping-mode AFM and TEM were used to investigate the effect of cyanobiphenyl side-chain mesogens in the block copolymers on the nanomorphologies of thin films. Figure 2S in the SI displays the AFM images of P3HT, P3HT$_{44}$-*b*-PTcbp$_5$, and P3HT$_{44}$-*b*-PTcbp$_7$ thin films casted from CF and DCB solutions. It was obvious that coarse and donutlike structures appeared in the thin films casted from CF; on the contrary, the fine and weblike structures occurred in the thin films casted from DCB, mainly because of the low volatile nature of DCB. Solvent annealing is an effective means to obtain ordered structures for the polymer systems. Then we performed the DCB solvent annealing experiments. It could be noted that the well-defined and distinct nanofibrils developed after DCB solvent vapor annealing, especially for P3HT$_{44}$-*b*-PTcbp$_5$ (Figures 3 and 4). On the other hand, in order to further investigate the principle of the self-assembly of diblock copolymer bearing cyanobiphenyl side-chain mesogens, we also conducted the AFM measurements of P1 prepared by spin coating from a DCB solution and upon DCB solvent annealing in Figure 3S in the SI. From these results, we found that the P1 diblock copolymer could microphase-separate into orderly morphology with a high degree of crystallinity slightly induced by the nature of the diblock copolymer, illustrating that the P3HT-*b*-PTcbp rod−rod block copolymer chains could develop spontaneously to form clear microphase-separated nanopatterns with a high degree of crystallinity and also reflecting that cyanobiphenyl side-chain mesogens in the block copolymers could also drive the polymer chains into ordered self-assembly nanostructures.[42−47] It was interesting that P3HT$_{44}$-*b*-PTcbp$_5$ eventually revealed crystalline nanofibers characteristic with wider fiber dimensions of ∼20 nm width and longer lengths up to ∼200 nm compared with the P3HT$_{44}$-*b*-

Table 1. Optical Properties, Electrochemical Onset Potentials, and Energy Levels of P3HT and P3HT-*b*-PTcbp Block Copolymer Films with Various Block Ratios

polymer	λ_{max} (nm)	λ_{onset} (nm)	E_g^{opt}[a] (eV)	E_{ox}[b] (V)	HOMO[c] (eV)	E_{red}[d] (V)	LUMO[e] (eV)	E_g^{ec}[f] (eV)
P3HT	556	630	1.97	0.905	−5.305	−1.150	−3.250	2.055
$P3HT_{44}$-*b*-$PTcbp_5$	560	669	1.85	0.850	−5.250	−1.005	−3.395	1.855
$P3HT_{44}$-*b*-$PTcbp_7$	558	610	2.04	0.825	−5.225	−1.300	−3.100	2.125

[a]Calculated from the absorption edges of the polymer film, $E_g^{opt} = 1240/\lambda_{onset}$. [b]Onset potential of the oxidation peaks versus SCE. [c]The HOMO was obtained according to the empirical formula HOMO = $-(E_{ox}+4.4)$ eV. [d]Onset potential of the reduction peaks versus SCE. [e]The LUMO was obtained according to the empirical formula LUMO = $-(E_{red}+4.4)$ eV. [f]E_g^{ec} was calculated from LUMO − HOMO.

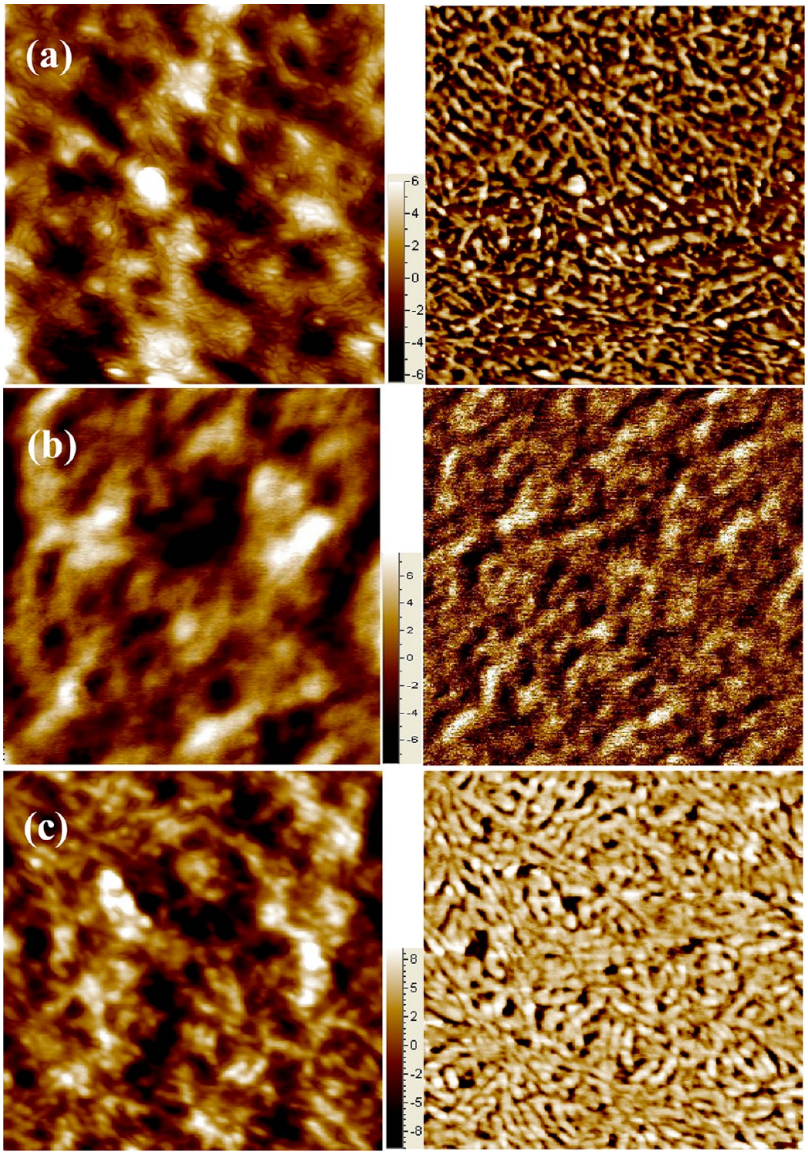

Figure 3. TE-AFM height (left) and phase (right) images of (a) P3HT, (b) $P3HT_{44}$-*b*-$PTcbp_5$, and (c) $P3HT_{44}$-*b*-$PTcbp_7$ films upon DCB solvent annealing. The image sizes were all 1 μm × 1 μm. All of the polymer concentrations were 10 mg/mL in the solutions.

$PTcbp_7$ thin films with ∼15 nm width and ∼100 nm length (Figure 4), indicating that significantly enhanced domain ordering and more favored crystalline domain orientations could be achieved when the amount of the cyanobiphenyl side-chain mesogens in the block copolymers was favorable. In addition, the nanoscale-ordered structures formed in the $P3HT_{44}$-*b*-$PTcbp_5$ and $P3HT_{44}$-*b*-$PTcbp_7$ block copolymer films might provide higher hole mobility and more stable hole-transport channels than pristine P3HT.

The transport of the hole within the electron donor phase would be strongly influenced by the molecular packing and crystallinity of the conjugated polymer chains in polymer solar cells.[48−50] The crystal structures of P3HT, $P3HT_{44}$-*b*-$PTcbp_5$, and $P3HT_{44}$-*b*-$PTcbp_7$ thin films were confirmed by XRD measurement, as shown in Figure 4S in the SI. It was observed that, compared with pristine P3HT, $P3HT_{44}$-*b*-$PTcbp_5$ and $P3HT_{44}$-*b*-$PTcbp_7$ showed a higher crystalline absorption peak at $2\theta \approx 6.3°$, corresponding to the (100) reflection, originating

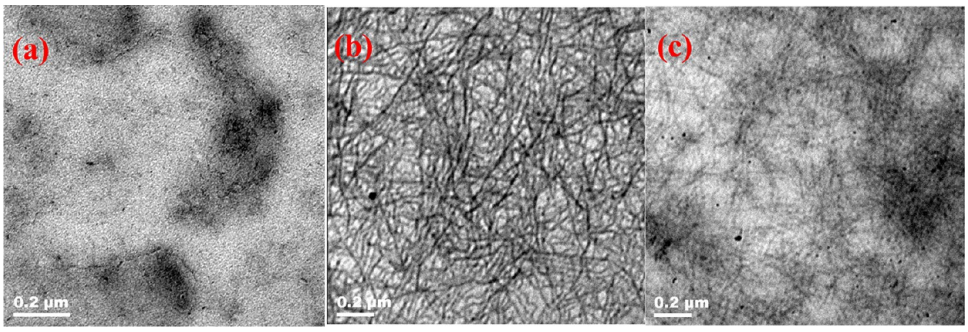

Figure 4. TEM images of (a) P3HT, (b) P3HT$_{44}$-*b*-PTcbp$_5$, and (c) P3HT$_{44}$-*b*-PTcbp$_7$ upon DCB solvent annealing. All of the polymer concentrations were 10 mg/mL in the solutions.

from the edge-on orientation of polymer chains with the thiophene ring parallel to the substrate, and an increased peak intensity of the (010) reflection, which arose from the intermolecular $\pi-\pi$-stacking characteristics among the thiophene backbone of the diblock copolymers, implying that cyanobiphenyl side-chain mesogens of the block copolymers could enhance the $\pi-\pi$-stacking interactions among the P3HT-*b*-PTcbp block copolymers. Meanwhile, the peak intensity at $2\theta \approx 6.3°$ of P3HT$_{44}$-*b*-PTcbp$_5$ was stronger than that of P3HT$_{44}$-*b*-PTcbp$_7$, revealing that excessive cyanobiphenyl side-chain mesogens might lead to an increase in the steric hindrance of block copolymer chains and restrict the movement and full stretch of the polymer chains. To gain further insight into the differences in the packing arrangements of the polymers, bulk SAXS of P3HT, P3HT$_{44}$-*b*-PTcbp$_5$, and P3HT$_{44}$-*b*-PTcbp$_7$ under DCB solvent annealing treatments for 12 h was processed. As shown in the inset of Figure 5, there were more outer rings appearing and a stronger reflection intensity in P3HT$_{44}$-*b*-PTcbp$_5$ and P3HT$_{44}$-*b*-PTcbp$_7$, especially for P3HT$_{44}$-*b*-PTcbp$_5$, compared with pristine P3HT, which might be indicative of the better nanoscale crystallization of the P3HT$_{44}$-*b*-PTcbp$_5$ block copolymer.[51] Furthermore, the 1D SAXS results were also included, where the P3HT, P3HT$_{44}$-*b*-PTcbp$_5$, and P3HT$_{44}$-*b*-PTcbp$_7$ films were measured at $q \approx 3.97$, 3.89, and 3.79 nm^{-1}, and the peak was correlative with intermolecular interactions, which would directly affect the transmission of the electron hole, and related to the optical and charge-transport properties in this electronic device.[52] There existed a slight blue shift in P3HT$_{44}$-*b*-PTcbp$_7$ (3.79 nm^{-1}) and P3HT$_{44}$-*b*-PTcbp$_5$ (3.89 nm^{-1}) compared with pristine P3HT (3.97 nm^{-1}), demonstrating that cyanobiphenyl side-chain mesogens would affect intermolecular $\pi-\pi$-stacking interactions and increase the distance between molecule chains among the thiophene rings.[53]

Cyclic voltammetry (CV) was usually employed to determine the lowest unoccupied molecular orbital (LUMO) and highest occupied molecular orbital (HOMO) energy levels of diblock copolymers.[54−56] The reduction potentials and onset oxidation obtained from CV measurement correspond to the LUMO and HOMO energy levels, respectively. Therefore, we investigated the electrochemical properties of P3HT, P3HT$_{44}$-*b*-PTcbp$_5$, and P3HT$_{44}$-*b*-PTcbp$_7$ (shown in Figure 5S in the SI) by CV measurement. The CV measurements were performed on a platinum electrode at a scan rate of 20 mV/s in an acetonitrile solution containing TBAPF$_6$ (0.1 mol/L) and using Ag/Ag$^+$ as the reference electrode. The corresponding optical and electric data were summarized in Table 1. The HOMO levels of P3HT, P3HT$_{44}$-*b*-PTcbp$_5$, and P3HT$_{44}$-*b*-PTcbp$_7$ were −5.305, −5.250, and −5.225 eV, and the LUMO levels were −3.250, −3.395, and −3.100 eV, respectively. The electrochemical band gap of P3HT$_{44}$-*b*-PTcbp$_5$ was measured to be 1.855 eV, which has a slight reduction compared with the values of P3HT (2.055 eV) and P3HT$_{44}$-*b*-PTcbp$_7$ (2.125 eV), implying that P3HT$_{44}$-*b*-PTcbp$_5$ would exhibit broader spectral absorption and eventually enhance the short-current density (J_{sc}) in the hybrid BHJ solar cells, in contrast with P3HT and P3HT$_{44}$-*b*-PTcbp$_7$. On the other hand, the valence (7.6 and 6.5

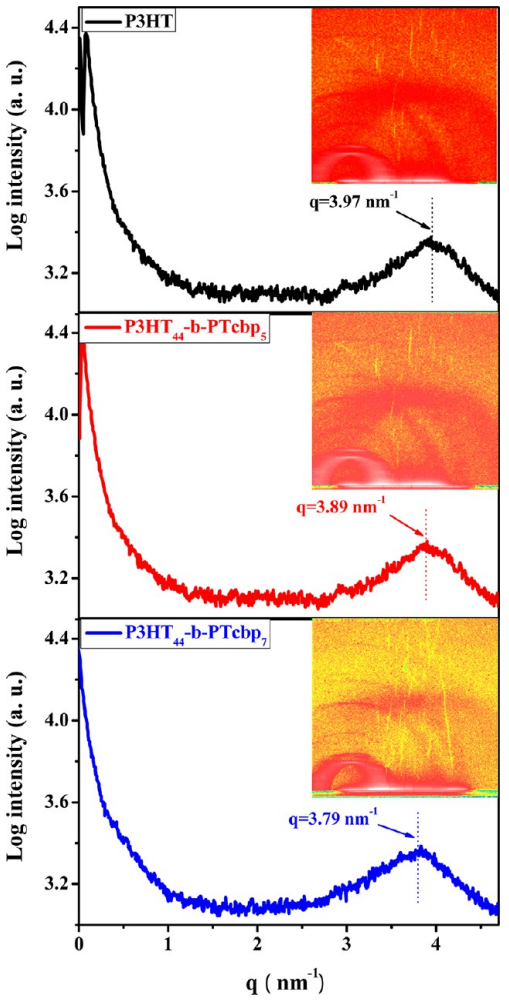

Figure 5. SAXS patterns of P3HT, P3HT$_{44}$-*b*-PTcbp$_5$, and P3HT$_{44}$-*b*-PTcbp$_7$ upon DCB solvent annealing. Inset: Corresponding 2D SAXS patterns of P3HT, P3HT$_{44}$-*b*-PTcbp$_5$, and P3HT$_{44}$-*b*-PTcbp$_7$ films. All of the polymer concentrations were 10 mg/mL in the solutions.

dx.doi.org/10.1021/am4033263 | ACS Appl. Mater. Interfaces 2013, 5, 11692−11702

eV) and conduction (4.4 and 3.6 eV) bands of ZnO and CdS, respectively, are displayed in Figure 6, revealing that effective

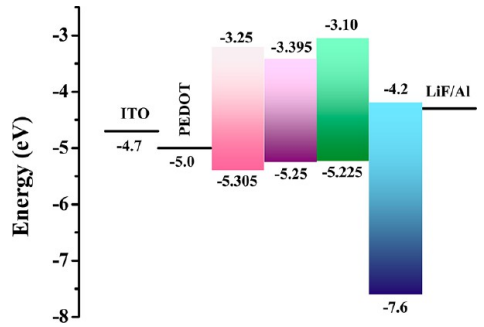

Figure 6. Energy-level diagram of the materials comprising the solar cell based on a P3HT and P3HT-*b*-PTcbp/ZnO active layer and the calculated HOMO/LUMO distributions of thiophene block copolymer donor materials.

exciton separation of those photoexcited polymers might occur at the polymer/ZnO and polymer/CdS interface via charge transfer, especially for the polymer/CdS hybrid system.

In our research, the hybrid system was comprised of P3HT-*b*-PTcbp and ZnO QDs modified by cbp liquid-crystalline ligands. Well-dispersion of ZnO QDs in a polymer matrix, intimate contact between the P3HT-*b*-PTcbp diblock copolymer and QD phases, and enhancement of the hybrid device performance were expected because of interaction between the cbp ligands on the surface of ZnO QDs and cyanobiphenyl side-chain mesogens of P3HT-*b*-PTcbp. The modification of ZnO QDs by cbp ligands was conducted overnight in a CF solution. The modified ZnO QDs were centrifuged twice in a CF solution to eliminate nonmodified ligand molecules and then redispersed in CF or DCB (Figure 6S in the SI). CdS QDs were also treated with the same process. ZnO modified by cbp was confirmed by FT-IR measurement, which showed that the cbp ligands were chemically linked to the surfaces of ZnO QDs (Figure 7S in the SI). Upon modification, the visible emission (or deep level emission) arising from the surface defect of ZnO was obviously depressed (Figure 8S in the SI), mainly attributing to the surface passivation of ZnO and the energy transfer between ZnO QDs and cbp ligands.[57−59] The physical conformation of the polymer chains can be inferred from the optical absorbance of the film. The normalized absorption spectra (Figure 7a) showed a wider main peak with increasing concentration of cbp@ZnO QDs with a fixed polymer concentration of 10 mg/mL, especially for a 1:2 weight proportion of the hybrid materials, due to the absorption of cyanobiphenyl side-chain mesogens of the diblock copolymer and cbp liquid-crystalline ligands. However, when the proportion of polymer and QDs was more than 1:2, the shoulder peak at ∼610 nm decreased significantly, revealing that an excessive amount of QDs might lead to disruption of the orderly arrangement of the polymer chains and restriction of the crystalline behavior. On the other hand, lower loading of QDs in a polymer matrix could limit the enhancement of J_{sc} because of the restricted *D*/*A* interface area, while higher loading of QDs in a polymer matrix could disrupt the orderly charge-transfer channel, which was also bad for improvement of the device performance instead. So, we conducted our device characterizations with 1:2 weight ratios of the polymer and QDs in the following tests. Figure 7b shows the normalized

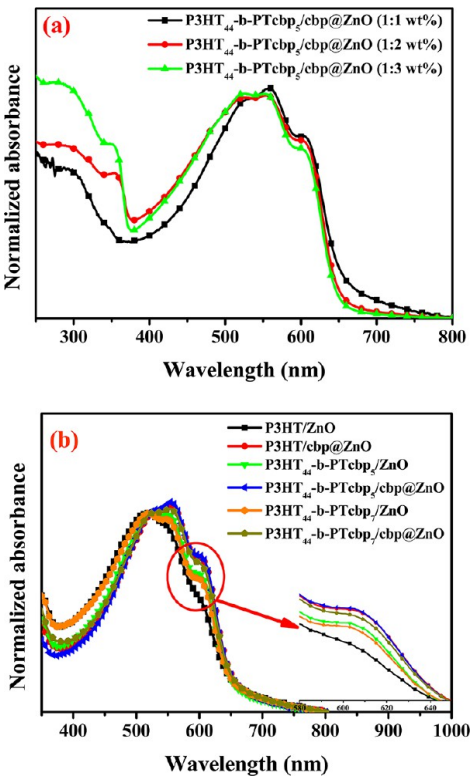

Figure 7. UV−vis absorption spectra of (a) $P3HT_{44}$-*b*-$PTcbp_5$/cbp@ZnO hybrid fims with different amounts of cbp@ZnO QDs, (b) P3HT/ZnO, $P3HT_{44}$-*b*-$PTcbp_5$/ZnO, $P3HT_{44}$-*b*-$PTcbp_7$/ZnO, P3HT/cbp@ZnO, $P3HT_{44}$-*b*-$PTcbp_5$/cbp@ZnO, and $P3HT_{44}$-*b*-$PTcbp_7$/cbp@ZnO nanocomposite films upon DCB solvent annealing (the proportion of polymer and QDs was 1:2, and the polymers were at a fixed concentration with 10 mg/mL).

UV−vis absorption spectra of polymer/ZnO and polymer/cbp@ZnO hybrid films (1:2 polymer/QDs) after DCB solvent vapor annealing for 12 h. The spectra of polymer/cbp@ZnO films displayed significant red shifts of the main peaks and an enhanced peak intensity at 610 nm compared with the polymer/ZnO films, indicating that intermolecular interactions between the cbp ligands of ZnO QDs and cyanobiphenyl side-chain mesogens of the P3HT-*b*-PTcbp block copolymers boosted the planarization effect of the π-conjugated P3HT-*b*-PTcbp polymer backbone and improved the ordered arrangement of the active layer in hybrid BHJ solar cells.[60]

PL measurements (Figure 8a) were further performed to investigate charge transfer between the P3HT-*b*-PTcbp diblock copolymer and QDs in the hybrid systems after DCB solvent vapor annealing. All of the blend films were excited at 460 nm, and the emission spectra were recorded in the range 550−800 nm. It was obvious that polymer/cbp@ZnO hybrids exhibited much more fluorescence quenching because of the fast deactivation of the excited state by the electron-transfer reaction, compared with polymer/ZnO QDs, proving the formation of intimate contact between the polymer and cbp@ZnO upon surface modification of ZnO QDs by cbp ligands. Meanwhile, a maximum of 85% of the fluorescence intensity quenched in the $P3HT_{44}$-*b*-$PTcbp_5$/cbp@ZnO hybrids, demonstrating the existence of more efficient photoinduced charge transfer between $P3HT_{44}$-*b*-$PTcbp_5$ and cbp@ZnO and a more ordered charge separation and transport path in the

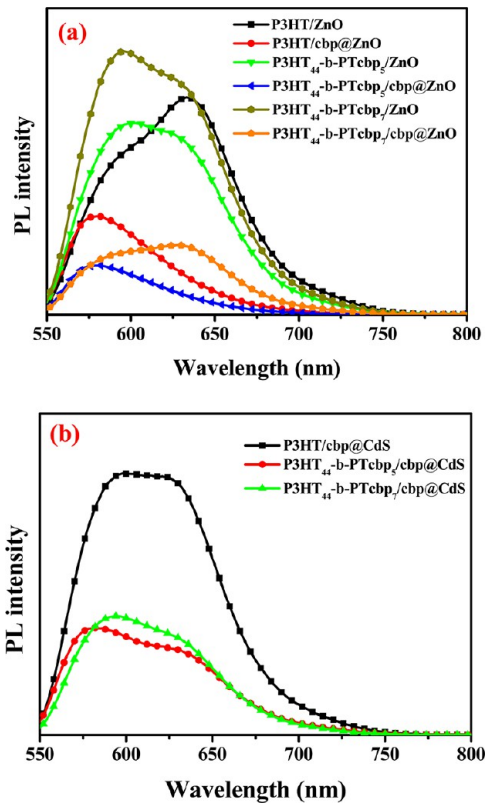

Figure 8. PL spectra of (a) polymer/cbp@ZnO- and (b) polymer/cbp@CdS-based nanocomposite films upon DCB solvent annealing. All of the proportions of polymer and QDs were 1:2, and the polymers were at a fixed concentration with 10 mg/mL.

hybrids,[61−64] similar to the PL results of P3HT-*b*-PTcbp/CdS hybrid systems (Figure 8b).

The morphology of the polymer/ZnO blends had a considerable impact on the efficiency of hybrid BHJ solar cells. TEM was performed to analyze the morphology of polymer/ZnO and polymer/cbp@ZnO hybrid films (Figure 9). We could observe the self-assembly and fine dispersion of cbp@ZnO in a diblock copolymer matrix due to the high miscibility between cbp ligands on the surface of ZnO QDs and cyanobiphenyl side-chain mesogenic pendants in block copolymers for structural similarity.[65] In addition, the TEM images displayed there only exhibited cbp@ZnO QDs well-dispersion in a P3HT matrix (Figure 9b), while the rodlike cbp@ZnO QDs with ∼5 nm width and ∼50 nm length, composed of ZnO nanoparticles (the size of the ZnO nanoparticles varied in a range of 3−8 nm) observed in the high-resolution TEM (HRTEM; Figure 9e), were self-assembled and highly controllably dispersed on the polymer nanofiber surface (Figure 9d). On the other hand, the outer rings in the electron diffraction patterns (insets) were from cbp@ZnO QDs, and the rings became stronger in P3HT-*b*-PTcbp/cbp@ZnO compared with P3HT/cbp@ZnO, implying that P3HT-*b*-PTcbp could contribute to the self-assembly of cbp@ZnO and increase the crystallinity of ZnO and interaction among cbp@ZnO QDs. The AFM and SEM images of the P3HT/cbp@ZnO, P3HT$_{44}$-*b*-PTcbp$_5$/cbp@ZnO, and P3HT$_{44}$-*b*-PTcbp$_7$/cbp@ZnO hybrid films also indicated that the dispersion of cbp@ZnO QDs was more uniform in the block copolymer matrix compared with the P3HT/ZnO hybrid film (Figures 9S and 10S in the SI), which was consistent with the results of P3HT-*b*-PTcbp/cbp@CdS hybrid systems (Figure 11S in the SI).

Photovoltaic devices had been fabricated by a structure of ITO/PEDOT:PSS/block copolymers:ZnO/LiF/Al. Devices all displayed typical diodelike $J-V$ curves under simulated solar illumination (100 mW/cm^2, AM1.5G; Figure 10A), and detailed results are given in Table 2. Compared with the polymer/ZnO devices, the FF, V_{oc}, and J_{sc} of polymer/cbp@ZnO cells were considerably enhanced. The high V_{oc} might be attributed to the introduction of cbp ligands on the ZnO surface. The larger J_{sc} was ascribed to an increase in charge-carrier generation and a decrease in charge recombination in the active layer, resulting from the more intimate mixing and enhancement in the intermolecular interactions between polymer chains and the planarization effect of a π-conjugated polymer backbone. The presence of these liquid-crystalline side chains improved the molecular orientation of the polythiophene block copolymer, resulting high crystallinity with nanofibril structure on dimensions below the exciton diffusion length, and allowed well-dispersion and the self-assembly of QDs in a polymer matrix, thus enhancing the formation of an interpenetrating network of QDs to enhance charge-carrier transport and collection at the electrode, which could also prevent charge recombination. The superior FF might result from the cooperative interaction between the cbp ligands on the surface of ZnO QDs and cyanobiphenyl mside-chain esogens of block copolymers, which would obtain a smoother and ordered active layer. P3HT$_{44}$-*b*-PTcbp$_5$/cbp@ZnO (power conversion efficiency PCE = 0.97) demonstrated the best photovoltaic performance, which might result from the broader absorption, formation of the ordered path for charge-carrier transport to the electrodes originating from the high crystalline and oriented nanofibrils,[54] and decrease of charge recombination due to the intimate interface between the polymer and QDs in nanoscales. Therefore, this was reasonably and importantly advocated by the orientation of cyanobiphenyl side-chain mesogens and the cooperative interaction between the polymer and QDs. We found that the device performance could be further improved by changing the band gap of QDs (Figure 10D). Through full optimization of the active layer, the best device, prepared by blending P3HT$_{44}$-*b*-PTcbp$_5$ (electron donors) and CdS QDs modified by cbp liquid-crystaline ligands (cbp@CdS; electron acceptors) with wider light absorption, reached an overall PCE of 2.3%, with V_{oc} = 0.77 V, J_{sc} = 5.5 mA/cm^2, and FF = 0.55, which highlighted the great potential of the hybrid active layer to realize high-performance hybrid BHJ solar cells by taking advantage of the driving by the cooperative interaction between the polymer and QDs and highly oriented nanofiber domains. The external quantum efficiency (EQE) spectra of devices based on P3HT$_{44}$-*b*-PTcbp$_5$/ZnO, P3HT$_{44}$-*b*-PTcbp$_5$/cbp@ZnO, and P3HT$_{44}$-*b*-PTcbp$_5$/cbp@CdS are shown in Figure 10C. The devices with polymer/cbp@QDs exhibited higher values, ranging from 400 to 700 nm, than those with pure QDs, which was in line with the results of device performances.

5. CONCLUSIONS

In summary, we have designed and synthesized conjugated rod−rod polythiophene diblock copolymers P3HT-*b*-PTcbp bearing cyanobiphenyl side-chain mesogens in one of polythiophene segments. Upon DCB solvent vapor annealing, the covalent bond between P3HT and PTcbp not only allows for the formation of an ordered microstructure on nanoscales

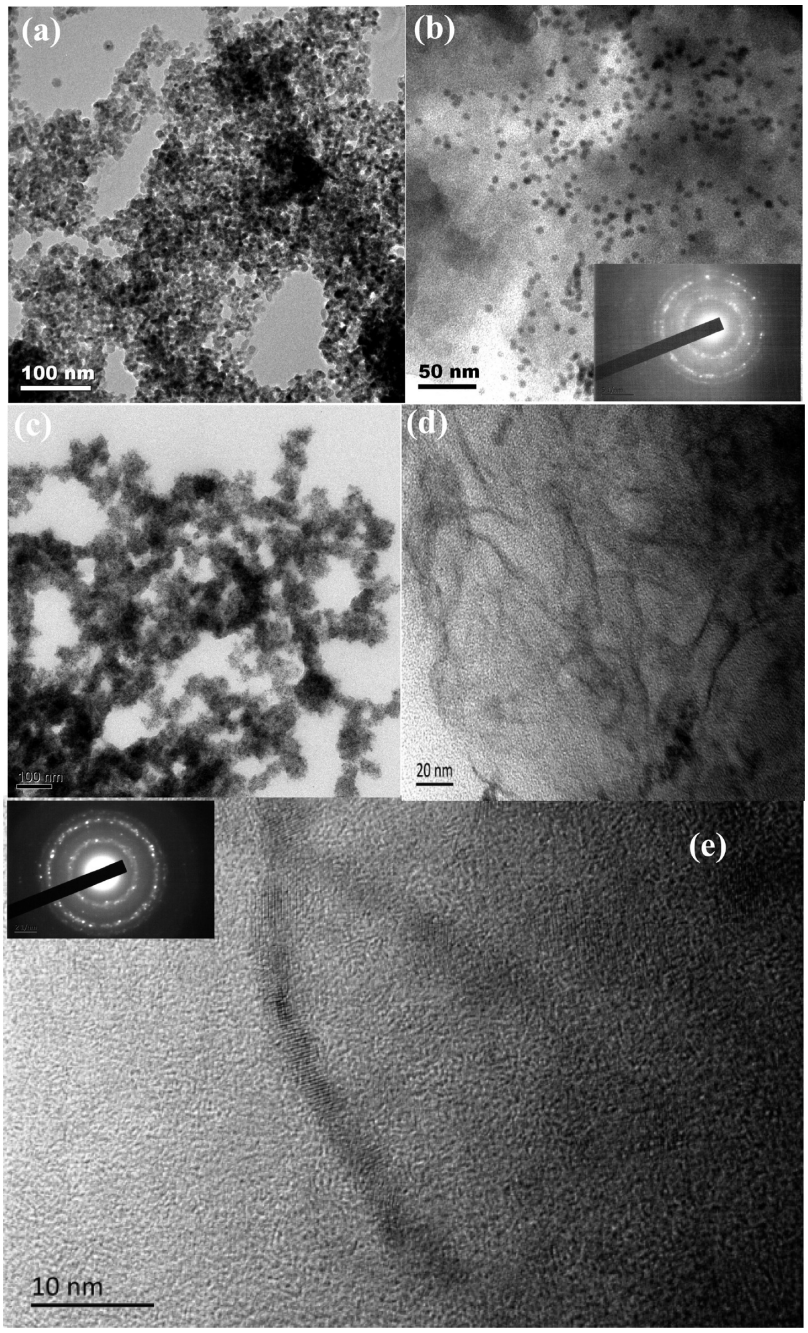

Figure 9. TEM images of (a) P3HT/ZnO, (b) P3HT/cbp@ZnO (c) P3HT-*b*-PTcbp/ZnO, and (d) P3HT-*b*-PTcbp/cbp@ZnO. (e) HRTEM images of the self-assembly of cbp@ZnO in the corresponding areas of P3HT-*b*-PTcbp/cbp@ZnO. All films undergo DCB solvent annealing. The insets are selected-area electron diffraction patterns of cbp@ZnO QDs in the corresponding areas of P3HT/cbp@ZnO and P3HT-*b*-PTcbp/cbp@ZnO. All of the proportions of polymer and QDs were 1:2, and the polymers were at a fixed concentration with 10 mg/mL.

but also leads to self-assembly into high crystalline and oriented nanofibrils on a length scale of exciton diffusion (10−20 nm), induced by the orientation of cyanobiphenyl side-chain mesogens and crystallization of P3HT and PTcbp blocks. It was the first time to investigate their photovoltaic performance using P3HT-*b*-PTcbp as electron donors and ZnO and CdS QDs modified by the cbp liquid-crystalline ligands (cbp@ZnO and cbp@CdS) as electron acceptors. Interestingly, we found the cooperative assembly and controllable well-dispersion of ZnO QDs modified by cbp ligands (cbp@ZnO) in the polymer nanofiber matrix because cbp@ZnO shows high miscibility with the P3HT-*b*-PTcbp block copolymer containing cyanobiphenyl side-chain mesogens for their structural similarity. Overall, the interaction between the donor and acceptor in the active layer has led to an improved photovoltaic performance resulting from the enhanced crystalline domain orientation, highly efficient transport pathways, and more intimately contacted polymer−QD nanocomposites of hybrid BHJ morphology. In addition, the best device of P3HT-*b*-PTcbp (electron donors) and CdS QDs modified by cbp liquid-crystaline ligands (cbp@CdS; electron acceptors) reached an overall PCE of 2.3%. More importantly, this method could pave the way to the optimization of high-performance photovoltaic devices because

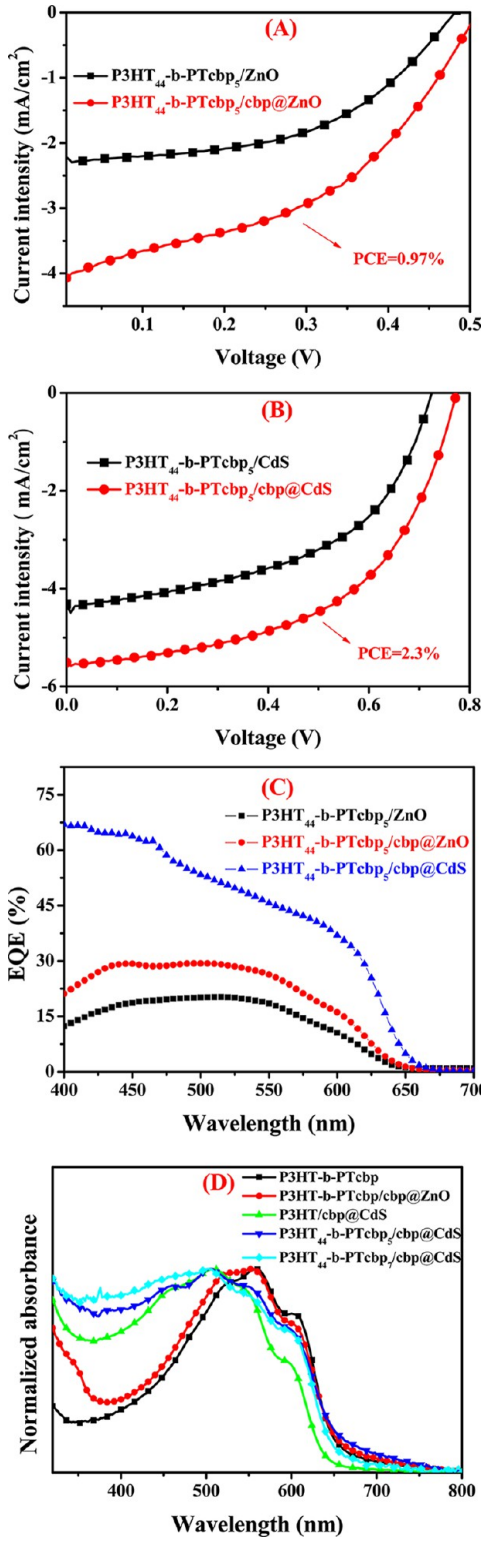

Figure 10. Current−voltage characteristics of (A) P3HT$_{44}$-*b*-PTcbp$_5$/ZnO- and P3HT$_{44}$-*b*-PTcbp$_5$/cbp@ZnO-based devices, (B) P3HT$_{44}$-*b*-PTcbp$_5$/CdS- and P3HT$_{44}$-*b*-PTcbp$_5$/cbp@CdS-based devices with DCB solvent annealing. Standard cells ITO/PEDOT:PSS/active layer/Al were fabricated, and the donor polymer concentrations were all 10 mg/mL in the active-layer solutions. (C) EQE spectra of P3HT$_{44}$-*b*-PTcbp$_5$/ZnO-, P3HT$_{44}$-*b*-PTcbp$_5$/cbp@ZnO-, and P3HT$_{44}$-*b*-PTcbp$_5$/cbp@CdS-based devices, and UV−vis absorption spectra of P3HT-*b*-PTcbp/cbp@CdS-based active layers compared with pure P3HT-*b*-PTcbp and P3HT-*b*-PTcbp/cbp@ZnO.

Table 2. Characteristic Current−Voltage Parameters of Solar Cells Based on P3HT/ZnO, P3HT/cbp@ZnO, P3HT-*b*-PTcbp/ZnO, P3HT-*b*-PTcbp/cbp@ZnO, P3HT/CdS, P3HT/cbp@CdS, P3HT-*b*-PTcbp/CdS, and P3HT-*b*-PTcbp/cbp@CdS

device	V_{oc} (V)	J_{sc} (mA/cm^2)	FF	PCE
P3HT/ZnO	0.49	1.9	0.40	0.37 ± 0.1
P3HT/cbp@ZnO	0.53	2.51	0.35	0.46 ± 0.1
P3HT$_{44}$-*b*-PTcbp$_5$/ZnO	0.48	2.4	0.50	0.58 ± 0.1
P3HT$_{44}$-*b*-PTcbp$_5$/cbp@ZnO	0.51	3.8	0.50	0.97 ± 0.2
P3HT$_{44}$-*b*-PTcbp$_7$/ZnO	0.46	2.0	0.40	0.37 ± 0.1
P3HT$_{44}$-*b*-PTcbp$_7$/cbp@ZnO	0.5	2.9	0.49	0.71 ± 0.2
P3HT/CdS	0.71	2.9	0.39	0.8 ± 0.1
P3HT/cbp@CdS	0.7	4.5	0.44	1.4 ± 0.1
P3HT$_{44}$-*b*-PTcbp$_5$/CdS	0.73	4.32	0.43	1.36 ± 0.1
P3HT$_{44}$-*b*-PTcbp$_5$/cbp@CdS	0.77	5.5	0.55	2.33 ± 0.2
P3HT$_{44}$-*b*-PTcbp$_7$/CdS	0.72	3.8	0.46	1.26 ± 0.1
P3HT$_{44}$-*b*-PTcbp$_7$/cbp@CdS	0.75	5.1	0.53	2.03 ± 0.1

V_{oc} is the open-circuit voltage. J_{sc} is the short-circuit current. The fill factor (FF) is a graphic measure of the squareness of the *J*−*V* curve. These parameters correspond to a simulated AM1.5G solar radiation under a N_2 atmosphere with an incident power density of 100 mW/cm^2.

of the highly oriented nanofiber domains and the special cooperative interaction between the polymer and QDs.

■ ASSOCIATED CONTENT

Ⓢ Supporting Information

Detailed experimental procedures, NMR, FT-IR, and PL spectra, AFM and SEM images, XRD patterns, and cyclic voltammograms. This material is available free of charge via the Internet at http://pubs.acs.org.

■ AUTHOR INFORMATION

Corresponding Author

*Tel.: +86 791 83969562. Fax: +86 791 83969561. E-mail: ywchen@ncu.edu.cn.

Notes

The authors declare no competing financial interest.

■ ACKNOWLEDGMENTS

Financial support for this work was provided by the National Natural Science Foundation of China (Grants 51073076, 51273088, 51172103, and 51302130).

■ REFERENCES

(1) Zhao, L.; Lin, Z. *Adv. Mater.* **2012**, *24*, 4353−4368.
(2) Borchert, H. *Energy Environ. Sci.* **2010**, *3*, 1682−1694.
(3) Reiss, P.; Couderc, E.; Girolamo, J. D.; Pron, A. *Nanoscale* **2011**, *3*, 466−489.
(4) Moulé, A. J.; Chang, L.; Thambidurai, C.; Vidu, R.; Stroeve, P. *J. Mater. Chem.* **2012**, *22*, 2351−2368.
(5) Zorn, M.; Bae, W. K.; Kwak, J.; Lee, H.; Lee, C.; Zentel, R.; Char, K. *ACS Nano* **2009**, *3*, 1063−1068.
(6) Alivisatos, A. P. *Science* **1996**, *271*, 933−937.
(7) Medintz, I. L.; Uyeda, H. T.; Goldman, E. R.; Mattoussi, H. *Nat. Mater.* **2005**, *4*, 435−446.
(8) Xu, J.; Xia, J.; Lin, Z. *Angew. Chem., Int. Ed.* **2007**, *46*, 1860−1863.
(9) Huynh, W. U.; Dittmer, J. J.; Alivisatos, A. P. *Science* **2002**, *295*, 2425−2427.

(10) Jun, Y. W.; Lee, S. M.; Kang, N. J.; Cheon, J. *J. Am. Chem. Soc.* **2001**, *123*, 5150−5151.
(11) Greene, L. E.; Law, M.; Tan, D. H.; Montano, M.; Goldberger, J.; Somorjai, G.; Yang, P. D. *Nano Lett.* **2005**, *5*, 1231−1236.
(12) Lauhon, L. J.; Gudiksen, M. S.; Wang, C. L.; Lieber, C. M. *Nature* **2002**, *420*, 57−61.
(13) Milliron, D. J.; Hughes, S. M.; Cui, Y.; Manna, L.; Li, J. B.; Wang, L. W.; Alivisatos, A. P. *Nature* **2004**, *430*, 190−195.
(14) Cho, K. S.; Talapin, D. V.; Gaschler, W.; Murray, C. B. *J. Am. Chem. Soc.* **2005**, *127*, 7140−7147.
(15) Jun, Y.-W.; Chung, H.-W.; Jang, J.-T.; Cheon, J. *J. Mater. Chem.* **2011**, *21*, 10283−10286.
(16) Manna, L.; Milliron, D. J.; Meisel, A.; Scher, E. C.; Alivisatos, A. P. *Nat. Mater.* **2003**, *2*, 382−385.
(17) Goodman, M. D.; Zhao, L.; DeRocher, K. A.; Wang, J.; Mallapragada, S. K.; Lin, Z. *ACS Nano* **2010**, *4*, 2043−2050.
(18) Thorkelsson, K.; Mastroianni, A. J.; Ercius, P.; Xu, T. *Nano Lett.* **2012**, *12*, 498−504.
(19) Li, L.; Hollinger, J.; Coombs, N.; Petrov, S.; Seferos, D. S. *Angew. Chem., Int. Ed.* **2011**, *50*, 8148−8152.
(20) Rahimi, K.; Botiz, I.; Stingelin, N.; Kayunkid, N.; Sommer, M.; Koch, F. P. V.; Nguyen, H.; Coulembier, O.; Dubois, P.; Brinkmann, M.; Reiter, G. *Angew. Chem., Int. Ed.* **2012**, *51*, 11131−11135.
(21) Zou, B. J.; Liu, L.; Chen, H.; Khondaker, S. I.; McCullough, R. D.; Huo, Q.; Zhai, L. *Adv. Mater.* **2008**, *20*, 2055−2060.
(22) Yen, W.-C.; Lee, Y.-H.; Lin, J.-F.; Dai, C.-A.; Jeng, U.-S.; Su, W.-F. *Langmuir* **2011**, *27*, 109−115.
(23) Günes, S.; Neugebauer, H.; Sariciftci, N. S. *Chem. Rev.* **2007**, *107*, 1324−1338.
(24) Lin, Y.; Daga, V. K.; Anderson, E. R.; Gido, S. P.; Watkins, J. J. *J. Am. Chem. Soc.* **2011**, *133*, 6513−6516.
(25) Lin, Y.; Wei, Q.; Qian, G.; Yao, L.; Watkins, J. J. *Macromolecules* **2012**, *45*, 8665−8673.
(26) Krüger, R. A.; Gordon, T. J.; Baumgartner, T.; Sutherland, T. C. *ACS Appl. Mater. Interfaces* **2011**, *3*, 2031−2041.
(27) Liu, J.; Tanaka, T.; Sivula, K.; Alivisatos, A. P.; Fréchet, J. M. J. *J. Am. Chem. Soc.* **2004**, *126*, 6550−6551.
(28) Kochemba, W. M.; Pickel, D. L.; Sumpter, B. G.; Chen, J.; Kilbey, S. M. *Chem. Mater.* **2012**, *24*, 4459−4467.
(29) Nagano, S.; Koizuka, Y.; Murase, T.; Sano, M.; Shinohara, Y.; Amemiya, Y.; Seki, T. *Angew. Chem., Int. Ed.* **2012**, *51*, 5884−5888.
(30) Broer, D. J.; Bastiaansen, C. M. W.; Debije, M. G.; Schenning, A. P. H. J. *Angew. Chem., Int. Ed.* **2012**, *51*, 7102−7109.
(31) Yu, H.; Kobayashi, T.; Yang, H. *Adv. Mater.* **2011**, *23*, 3337−3344.
(32) Tong, X.; Han, D.; Fortin, D.; Zhao, Y. *Adv. Funct. Mater.* **2013**, *23*, 204−208.
(33) Mavundla, S. E.; Malgas, G. F.; Motaung, D. E.; Iwuoha, E. I. *J. Mater. Sci.* **2012**, *47*, 5455−5460.
(34) Beek, W. J. E.; Wienk, M. M.; Kemerink, M.; Yang, X.; Janssen, R. A. J. *J. Phys. Chem. B* **2005**, *109*, 9505−9516.
(35) Oosterhout, S. D.; Koster, L. J. A.; van Bavel, S. S.; Loos, J.; Stenzel, O.; Thiedmann, R.; Schmidt, V.; Campo, B.; Cleij, T. J.; Lutzen, L.; Vanderzande, D.; Wienk, M. M.; Janssen, R. A. J. *Adv. Energy Mater.* **2011**, *1*, 90−96.
(36) Olson, D. C.; Lee, Y. J.; White, M. S.; Kopidakis, N.; Shaheen, S. E.; Ginley, D. S.; Voigt, J. A.; Hsu, J. W. P. *J. Phys. Chem. C* **2007**, *111*, 16640−16645.
(37) Steyrleuthner, R.; Schubert, M.; Howard, I.; Klaumünzer, B.; Schilling, K.; Chen, Z.; Saalfrank, P.; Laquai, F.; Facchetti, A.; Neher, D. *J. Am. Chem. Soc.* **2012**, *134*, 18303−18317.
(38) Chueh, C.-C.; Higashihara, T.; Tsai, J.-H.; Ueda, M.; Chen, W.-C. *Org. Electron.* **2009**, *10*, 1541−1548.
(39) Yi, Z.; Sun, X.; Zhao, Y.; Guo, Y.; Chen, X.; Qin, J.; Yu, G.; Liu, Y. *Chem. Mater.* **2012**, *24*, 4350−4356.
(40) Ku, S.-Y.; Brady, M. A.; Treat, N. D.; Cochran, J. E.; Robb, M. J.; Kramer, E. J.; Chabinyc, M. L.; Hawker, C. J. *J. Am. Chem. Soc.* **2012**, *134*, 16040−16046.
(41) Choi, S. Y.; Lee, J. U.; Lee, J. W.; Lee, S.; Song, Y. J.; Jo, W. H.; Kim, S. H. *Macromolecules* **2011**, *44*, 1771−1774.
(42) Park, B. S.; Lee, D. H.; Russell, T. P. *Adv. Mater.* **2010**, *22*, 1882−1884.
(43) Zhang, Q.; Cirpan, A.; Russell, T. P.; Emrick, T. *Macromolecules* **2009**, *42*, 1079−1082.
(44) Gu, W.; Hong, S. W.; Russell, T. P. *ACS Nano* **2012**, *6*, 10250−10257.
(45) Xu, B. J.; Park, S.; Wang, S.; Russell, T. P.; Ocko, B. M.; Checco, A. *Adv. Mater.* **2010**, *22*, 2268−2272.
(46) Yang, S. K.; Ambade, A. V.; Weck, M. *Chem. Soc. Rev.* **2011**, *40*, 129−137.
(47) Kim, Y.; Cook, S.; Tuladhar, S. M.; Choulis, S. A.; Nelson, J.; Durrant, J. R.; Bradley, D. D. C.; Giles, M.; McCulloch, I.; Ha, C.-S.; Ree, M. *Nat. Mater.* **2006**, *5*, 197−203.
(48) Brabec, C. J.; Heeney, M.; McCulloch, I.; Nelson, J. *Chem. Soc. Rev.* **2011**, *40*, 1185−1199.
(49) Park, Y. D.; Park, J. K.; Seo, J. H.; Yuen, J. D.; Lee, W. H.; Cho, K.; Bazan, G. C. *Adv. Energy Mater.* **2011**, *1*, 63−67.
(50) Yi, Z.; Sun, X.; Zhao, Y.; Guo, Y.; Chen, X.; Qin, J.; Yu, G.; Liu, Y. *Chem. Mater.* **2012**, *24*, 4350−4356.
(51) Perret, E.; Reifler, F. A.; Hufenus, R.; Bunk, O.; Heuberger, M. *Macromolecules* **2013**, *46*, 440−448.
(52) Ho, V.; Boudouris, B. W.; McCulloch, B. L.; Shuttle, C. G.; Burkhardt, M.; Chabinyc, M. L.; Segalman, R. A. *J. Am. Chem. Soc.* **2011**, *133*, 9270−9273.
(53) Piliego, C.; Holcombe, T. W.; Douglas, J. D.; Woo, C. H.; Beaujuge, P. M.; Fréchet, J. M. J. *J. Am. Chem. Soc.* **2010**, *132*, 7595−7597.
(54) Liu, B.; Chen, X.; Zou, Y.; Xiao, L.; Xu, X.; He, Y.; Li, L.; Li, Y. *Macromolecules* **2012**, *45*, 6898−6905.
(55) Hu, X.; Zuo, L.; Fu, W.; Larsen-Olsen, T. T.; Helgesen, M.; Bundgaard, E.; Hagemann, O.; Shi, M.; Krebs, F. C.; Chen, H. *J. Mater. Chem.* **2012**, *22*, 15710−15716.
(56) Zhang, Y.; Zou, J.; Cheuh, C.-C.; Yip, H.-L.; Jen, A. K.-Y. *Macromolecules* **2012**, *45*, 5427−5435.
(57) Li, F.; Shi, Y.; Yuan, K.; Chen, Y. *New J. Chem.* **2013**, *37*, 195−203.
(58) Zeng, H.; Duan, G.; Li, Y.; Yang, S.; Xu, X.; Cai, W. *Adv. Funct. Mater.* **2010**, *20*, 561−572.
(59) Tian, J.; Zhang, Q.; Zhang, L.; Gao, R.; Shen, L.; Zhang, S.; Qu, X.; Cao, G. *Nanoscale* **2013**, *5*, 936−943.
(60) Ong, B. S.; Wu, Y.; Liu, P.; Gardner, S. *J. Am. Chem. Soc.* **2004**, *126*, 3378−3379.
(61) Stalder, R.; Xie, D.; Zhou, R.; Xue, J.; Reynolds, J. R.; Schanze, K. S. *Chem. Mater.* **2012**, *24*, 3143−3152.
(62) Xu, T.; Qiao, Q. *Energy Environ. Sci.* **2011**, *4*, 2700−2720.
(63) Treat, N. D.; Varotto, A.; Takacs, C. J.; Batara, N.; Al-Hashimi, M.; Heeney, M. J.; Heeger, A. J.; Wudl, F.; Hawker, C. J.; Chabinyc, M. L. *J. Am. Chem. Soc.* **2012**, *134*, 15869−15879.
(64) Ren, S.; Chang, L.-Y.; Lim, S.-K.; Zhao, J.; Smith, M.; Zhao, N.; Bulović, V.; Bawendi, M.; Gradečak, S. *Nano Lett.* **2011**, *11*, 3998−4002.
(65) Gu, Z.; Tan, Y.; Tsuchiya, K.; Shimomura, T.; Ogino, K. *Polymers* **2011**, *3*, 558−570.